Design of Flexible Wind Tunnel Model of Yawed Wind Turbine Rotor with Teetering Hub

Georgopoulos, P.; Sodja, J.; De Breuker, R.

DOI
10.2514/6.2023-2091

Publication date
2023

Document Version
Final published version

Published in
AIAA SciTech Forum 2023

AIAA SciTech Forum
23-27 January 2023, National Harbor, MD & Online
AIAA SCITECH 2023 Forum

10.2514/6.2023-2091

Design of Flexible Wind Tunnel Model of Yawed Wind Turbine Rotor with Teetering Hub

Panagiotis Georgopoulos*, Jurij Sodja† and Roeland De Breuker‡
Delft University of Technology, Faculty of Aerospace Engineering, Aerospace Structures and Materials, Kluyverweg 1, Delft, 2629 HS, The Netherlands

The present study regards a novel wind turbine design featuring a two-bladed rotor on a teetering hub and a yawed tower. A reduced order modelling methodology is proposed for the equation of motion, using a lumped parameter approximation to derive expressions for the structural, rotordynamic and geometric stiffness terms. The analytical expressions are validated numerically. In addition, a methodology is developed for aeroelastic scaling of the rotor for use in wind tunnel tests. This results in two blade design templates, a "stiff" and a "flexible" design focusing on the vibration behaviour and deflected shapes respectively. The templates are designed to be 3D-printable as a single part. Design optimisation was performed in MSC Nastran, yielding two rotor designs, each aiming to match the non-dimensional parameters of interest. The stiff rotor matches the flapwise and torsional natural frequencies within 2.7% error, but has a mismatch in the edgewise mode, as well as the modeshapes and anti-symmetric modes. The flexible rotor is capable of capturing the target normalised displacement profile, at reduced structural mass, partially alleviating the mismatch in Lock number.

I. Introduction

The past decade saw governments from all over the world committing to climate goals with ever increasing urgency, aiming to eliminate net emissions of greenhouse gases. This requires a drastic transition from fossil fuels to renewable energy sources, such as hydroelectric, solar and wind energy. An interesting subcategory of the latter is a floating, offshore installation. Unlike their offshore fixed-foundation counterparts, floating wind turbine positioning is not limited by water depth, allowing access to deeper waters and more favourable wind conditions. The list of advantages also includes cost savings due to the lack of a foundation structure, easier transport and maintenance via towing, as well as a less intrusive presence in the local ecosystem, among others [1].

In this context, TouchWind BV has proposed a floating offshore wind turbine concept. Their design differs from the conventional three-bladed horizontal axis wind turbine (HAWT) configuration in a variety of ways. Most notably, it incorporates a "yawed" tower and a two-bladed rotor on a teetering hub (2BTH). A key advantage of the yawed tower is to allow operation at higher wind speeds, minimising idle time for the turbine and hence increasing annual power production; this is achieved by allowing the tower to erect passively at increasing wind speeds, thereby maintaining the air flow through the projected rotor plane and hence the aerodynamic loads. This heavily yawed configuration introduces an aerodynamic load imbalance, as a result of the two blades moving upstream and downstream respectively. The teetering hub allows the rotor to pitch passively so as to equalise the moments along the hinge axis, hence alleviating fatigue loads at the hub. The concept is depicted in Fig. 1 [2].

Overall, the system's key characteristics, namely the yawed flow and teetering hub, have been individually investigated by numerous past studies. Yawed flow violates the requirement for axially aligned flow, which is a core assumption in blade element momentum (BEM) theory and so has drawn the attention of researchers, in an attempt to extend the method's applicability. Therefore, past studies have proposed corrections to account for this effect [3], [4]. In addition, yawed flow gives rise to other interesting aerodynamic phenomena, such as spanwise flow and dynamic stall, which remain underexplored. Hence studies typically investigate the pertinent aerodynamics in isolation, using simplified rigid blade structures, neglecting the effects of elasticity. Moreover, these studies are conducted on the conventional three-bladed HAWT configuration. With regards to the 2BTH configuration, the limited existing literature does not investigate the effects of yawed flow [5], [6], [7].

*PhD candidate, Aerospace Structures and Materials, p.georgopoulos@tudelft.nl, AIAA Student Member
†Assistant Professor, Aerospace Structures and Materials, j.sodja@tudelft.nl, AIAA Senior Member
‡Associate Professor, Aerospace Structures and Materials, r.debreuker@tudelft.n, AIAA Associate Fellowl

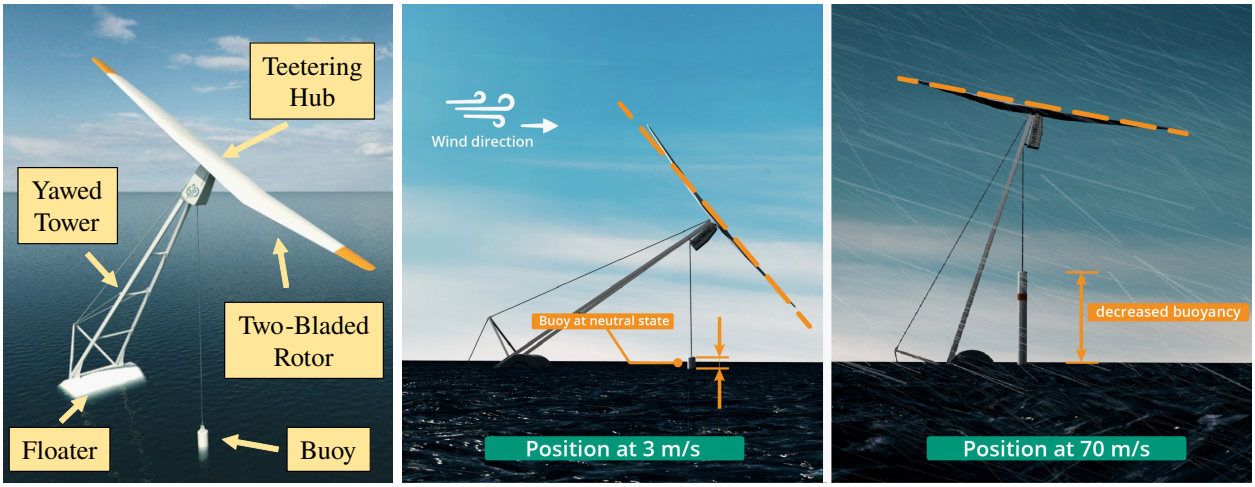

Figure 1 The TouchWind concept [2]

In the early stages of a wind turbine concept development, wind tunnel (WT) testing of a down-scaled prototype is a key tool in the up-scaling process. The repeatable operating conditions allow for precise measurements which are often not possible at full-scale (FS), as well as the exploration of the physical behaviour of the system at significantly lower cost. Results from the experiments can be used to calibrate numerical models, ultimately enabling upscaling. Traditionally, WT testing campaigns have focused on aerodynamic characterisation, with recent research expanding the scope of WT testing, to include aeroservoelasticity [8], [9]. Both studies were focused on the HAWT configuration, the former also addressing yawed flow. In both cases, composite blade designs were developed, aiming to minimise the offset from the non-dimensional parameter values predicted by scaling laws, as a result of an aerostructural optimisation.

The present study is conducted in the context of the project "TouchWind-PoP: Proof of principle for cost effective floating offshore wind turbine concept". The system's aerodynamics were modelled by Krishnan et al. [10] in a parallel study, by coupling a BEM approach to a rigid-body model of the rotor, accounting for rotation along the hinge axis and skewed wake effects. Therefore aerodynamic modelling is not considered in this paper; instead, this pa per has the following two areas of focus. First, a reduced order model (ROM) of the equations of motion (EoM) of a 2BTH wind turbine is developed. In the ROM, the rotor structure is modelled using a lumped parameter approximation, based on which analytical expressions for the rotordynamics and geometric stiffness are derived. Second, a scaling strategy for the design of a WT-scale 2BTH is proposed, including a set of assumptions and simplifications, ultimately resulting in two blade design templates. The design templates are intended for 3D-printing, further reducing testing costs as well as manufacturing complexity, as opposed to conventional designs made of balsa wood or composite materials. A design optimisation is performed to assess the applicability of the proposed templates.

The rest of this paper is organised as follows. Section II presents the ROM methodology, applying it on the FS model of the rotor. Section III presents the scaling strategy and developed blade design templates, followed by a description and numerical analysis of the optimised WT-scale rotors. Finally, Section IV highlights the conclusions from this study.

II. Modelling & Analysis Framework

A. Full-Scale Rotor Design

A conceptual, 30m-diameter FS rotor design is provided by the project partners, to be used as reference for the 1.2m-diameter WT-scale models. The rotor consists of two blades and a teetering hub. The blade planform has no pre-bend or pre-twist, featuring a single airfoil section NACA63618 with a maximum thickness 18%-chord at 34.7% chordwise position. The blade has a 12m span and a chord length of 3.4m and 1.13m at the root and tip respectively.

The blade section design evolves along its span, featuring three distinct regions: the "root" (0-2.25m), the "main blade" (2.25-11.5m) and the "tip" (11.5-12m). The root region acts as a transition stage from the hub to the blade featuring a "root connection laminate" made of a stiff tri-axial (Tri1200E, -45°/+45°/0°) glass-fibre fabric, which spans the entire section along the chord. The tip region is narrow enough such that the interior of the blade is completely filled

with PVC60 foam, facilitating the joining of the pressure and suction side shells. The majority of the blade span is characterised by the main blade region; a schematic is included in Fig. 2, highlighting the individual parts that constitute the cross-section of the blade. The blade consists of the pressure and suction side shells, which are connected along the leading edge (LE) and trailing edge (TE), as well as the blade's tip. Two "main shear webs" and one "trailing edge shear web" support the two shells throughout the root and main blade regions. The shear webs are sandwich panels made of bi-axial glass-fibre fabric (Bi800E, -45°/+45° - green) and a PVC60 foam core (pink). The shells consist primarily of two "girders" (main/trailing) of unidirectional glass-fibre (UD1200HM, 0° - blue) laminate oriented along the blade axis, upon which the shear webs are joined. The purpose of the former is to provide flapwise stiffness and are therefore positioned at 30%-chord, near the location of maximum thickness. The latter mainly facilitate joining the trailing shear web to the shells, hence they are significantly thinner and less wide than the main girders. The remaining area in the LE, TE and in-between the girders is filled with PVC60 foam. The girders and foam panels are enclosed on both sides by layers of tri-axial glass-fibre fabric (BiZero750E, -45°/+45°/0° - yellow) , making the shell a sandwich structure. The girders only span the main blade region. The fiber orientations mentioned above use the blade axis as the 0° orientation. For each shell the axis of rotation is defined normal to the blade, from inside out.

A detailed conceptual blade design is provided by the project partners, to provide a basis for numerical studies on the blade structure of the proposed concept. This is not the case for the 3m-radius hub structure, which is simplified to a beam of rectangular cross section (height 450mm, width 900mm, thickness 75mm), made of Tri1200E. In addition, a design for the shaft, gearbox, tower and floater is not provided by the project partners, therefore the present analysis is focused on the rotor.

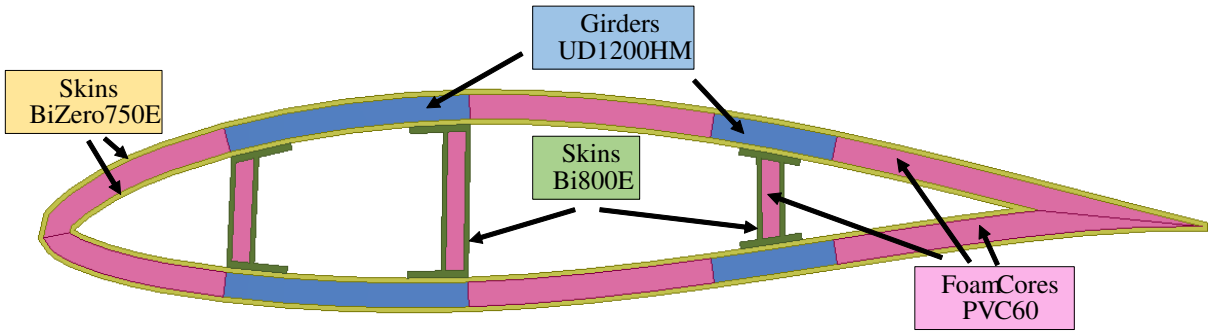

Figure 2 Schematic of the main blade section (not to scale)

The finite element (FE) model of the rotor structure is modelled in MSC Nastran, using an in-house MATLAB code which automatically generates the MSC Nastran input files. The entire blade structure is modelled using first-order 2D shell elements: quadrilateral (CQUAD4) for the flat shear webs and triangular (CTRIA3) for the curved shells. The hub is modelled using 1D beam elements (CBEAM) and is connected to the nodes on the blade root section via a rigid body element (RBE2). This modelling approach imparts artificially high stiffness to the shell of the root section, however it is made in the absence of a detailed description of the hub structure, given the fact that a detailed structural design of the hub would feature a stiff Tri1200E laminate. The skewed hinge is oriented at an angle $\gamma = 26.6^{\circ}$ relative to the blade axis and is defined in the FE model at the central node of the hub as a boundary condition, fixing all degrees-of-freedom (DoF) except rotation along the x-axis. The hinge node is defined using an alternative coordinate system whose x-axis is aligned with the hinge axis. The FS rotor model is presented in Fig. 3; its MATLAB-generated geometry is shown in Fig. 3a highlighting the orientation of the global (G) and hinge (H) coordinate systems with the corresponding FE model shown in Fig. 3b.

B. Equations of Motion

1. Overview

The EoM can be expressed in terms of the total mass matrix $[M]$, damping matrix $[B]$, stiffness matrix $[K]$ and the excitation force $\vec{f}$, as shown in Eq. (1). This classification is made based on whether a term is proportional to acceleration $\ddot{\vec{x}}$, velocity $\dot{\vec{x}}$ or displacement $\vec{x}$. The analysis is carried out in the rotational frame of reference (RFR). The individual matrices are the sum of numerous terms which are grouped into three main categories:

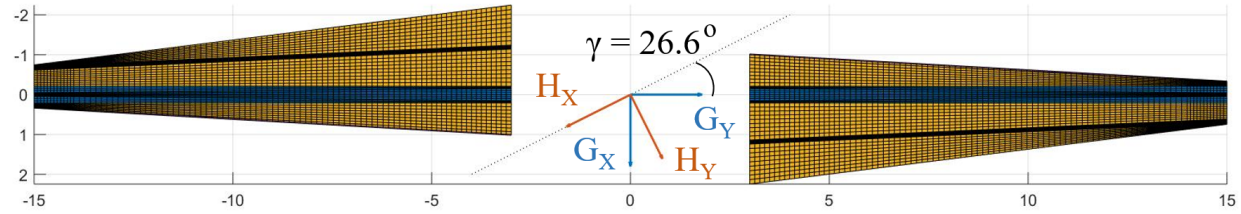

(a) MATLAB-generated geometric representation

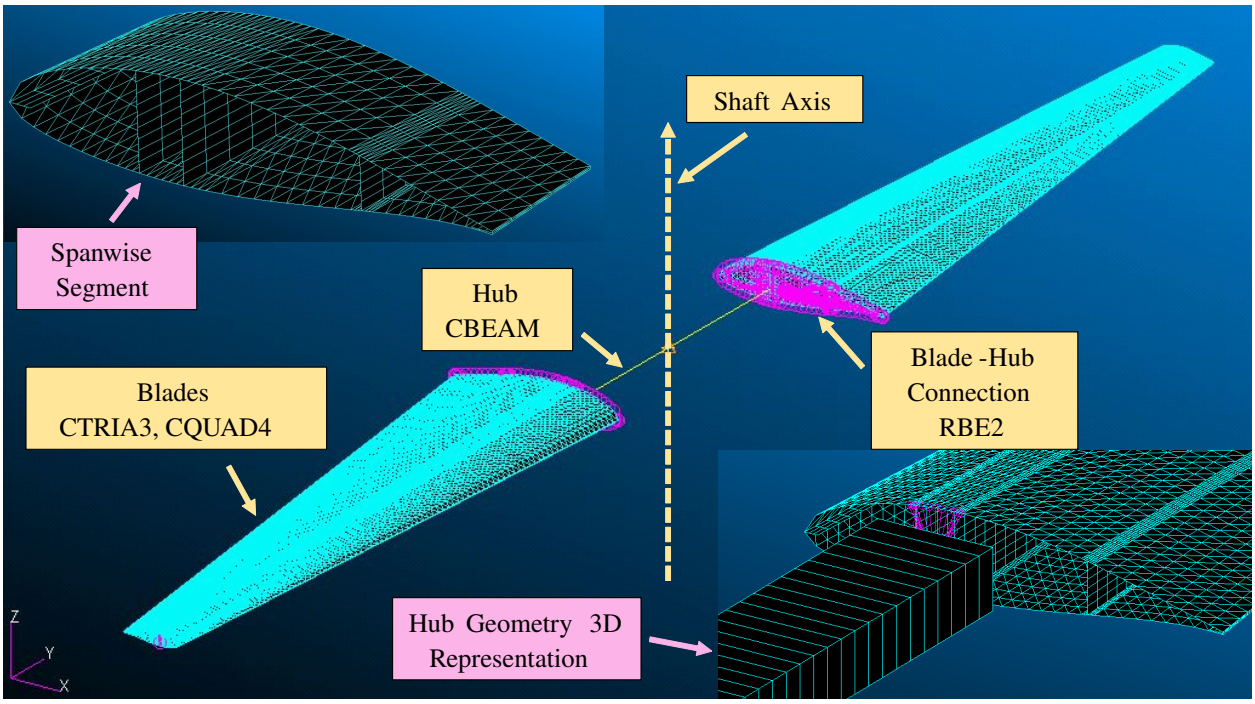

(b) MSC Nastran FE model

Figure 3 FS rotor model

$$[M]\ddot{\vec{x}} + [B]\dot{\vec{x}} + [K]\vec{x} = \vec{f} \tag{1}$$

- Structural: The structure's properties are captured numerically via the structural mass $[M_S]$ and stiffness $[K_S]$ matrices, which represent the inertial and elastic properties of the FE model. In the absence of experimental data, structural damping is modelled using an estimate for the damping factor of ζ= 0.5% [11]. Viscous damping is not included in the model.
- Rotordynamics: The choice to model the system in the RFR introduces the centrifugal stiffness $[K_{CE}]$ and Coriolis damping $[B_{CO}]$ matrices, as well as the centrifugal excitation force $f_{CE}^{\vec{exc}}$. These terms are functions of the rotational speed Ω.
- Aerodynamics: Aerodynamics modelling is not considered in this paper. Nevertheless, a model based on strip theory and Theodorsen's expressions for unsteady aerodynamics [12] could be coupled by introducing the aerodynamic mass matrix $[M_{AE}]$, damping matrix $[B_{AE}]$ and stiffness matrix $[K_{AE}]$, as well as the aerodynamic excitation force $f_{AE}^{\vec{exc}}$. In strip theory, the blade is split into discrete segments i for which the above aerodynamic terms are calculated. The normal and tangential induction values need to be derived in order to calculate the terms above; these terms reflect the change in wind speed as a result of the forces exerted by the blade segments to the air, thereby characterising wind turbine aerodynamics. The above aerodynamic terms are functions of the mode of operation, specifically Ω, wind speed V, tower yaw $\xi$and the rotor's azimuthal position ψ.

The EoM include two more terms which do not fall under one of these three categories. First is the gravitational

excitation force $f_{GR}^{\vec{exc}}$, which is a function of $\xi$and ψ. Second is the geometric stiffness matrix $[K_{GE}]$, which accounts for higher order strain in the structure and hence the displacement of the nodes (also known as "differential stiffness"). When all the above terms are accounted for, Eq. (1) is extended into Eq. (2).

$$([M_S] + [M_{AE}])\ddot{\vec{x}} + ([B_{CO}] + [B_{AE}])\dot{\vec{x}} + ((1 + i2\zeta)[K_S] + [K_{CE}] + [K_{AE}] + [K_{GE}])\vec{x} = f_{AE}^{\vec{exc}} + f_{CE}^{\vec{exc}} + f_{GR}^{\vec{exc}} \quad (2)$$

2. Reduced Order Structural Model

The FE model of the blade requires a refined mesh to effectively capture the curved geometry of the airfoil. A methodology is developed for the extraction of a ROM in MATLAB from the FE model, representing the rotor as a series of 6-DoF nodes along an axis. Specifically, each blade is modelled using 20 nodes, while each side of the hub is reduced to 3 nodes. Finally, the hinge mechanism is represented by a single 1-DoF node. Overall, the structure is reduced to a total of 47 nodes and 277 DoF, allowing computations in MATLAB at a reduced cost. It must be noted that the nodes do not represent the centre of gravity (CoG) or shear centre of the section, but simply act as reference points conveniently located along a line, as shown in Fig. 4. This formulation also facilitates the use of strip theory to model aerodynamics.

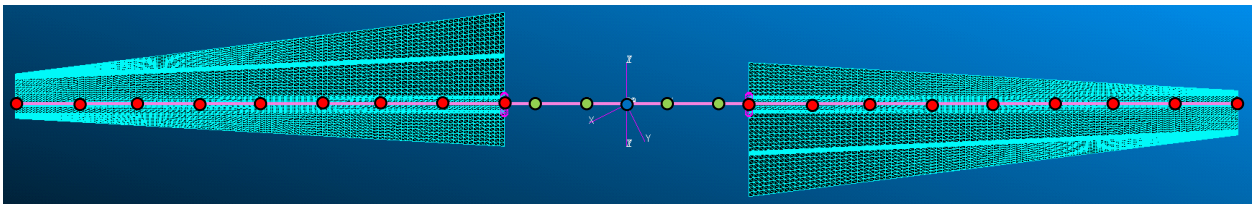

Figure 4 ROM of the rotor, represented as a series of 6-DoF nodes along a line

Common model reduction methods, such as Guyan reduction [13], utilise DoF from existing nodes to reduce the initial model to a smaller set of DoF of interest. Such an approach is not applicable in this case for two reasons. First, the structure does not feature nodes on the positions of interest along the blade axis, as this is empty space enclosed by the main girders and shear webs. Second, a single node cannot accurately represent the motion of a blade section in the case of this structure, due to the local deformations ("warping") observed under loading of the shell structure, which alter the geometry of the section. This is largely attributed to the uneven distribution of stiffness across the section, having stiff girders and shear webs grouped together and then using compliant PVC60 foam for the majority of the section periphery. Hence, the nodes on the main girders and shear webs are used to define reference nodes via interpolation elements (RBE3), representing the motion of the section. A blade segment is defined around each reference node, ultimately treating the blade as a series of such spanwise segments.

Having established the reference nodes, the reduced structural matrices $[\tilde{M}_S]$, $[\tilde{K}_S]$ can be extracted. The $[\tilde{M}_S]$ treats the structure as a series of N 6-by-6 concentrated mass/inertia elements $[\hat{M}_i]$, each such element corresponding to a single segment i, such that $i = 1, 2, \ldots, N$. Each $[\hat{M}_i]$ is extracted by isolating the segment of interest into an auxiliary FE model and then applying WEIGHTCHECK in MSC Nastran, with respect to the corresponding reference node. The 6-by-6 mass matrix is a function of the segment mass m, the distance from the reference node to the CoG $\{x_o, y_o, z_o\}$ and the segment's inertia tensor $[I]$ with respect to the reference node and the selected coordinate system, as shown in Eq. (3). The set of extracted $[\hat{M}_i]$ are combined to define $[\tilde{M}_S]$, relating inertial loads $\vec{\hat{f}}_i$ to the acceleration of the reference node $\ddot{\vec{\hat{x}}}_i$. The ROM force vector $\vec{\tilde{f}}$, as well as the acceleration vector $\ddot{\vec{\tilde{x}}}$ are assembled accordingly in Eq. (4) and Eq. (5).

$$[\hat{M}_i] = \begin{bmatrix} m & 0 & 0 & 0 & mz_o & -my_o \\ 0 & m & 0 & -mz_o & 0 & mx_o \\ 0 & 0 & m & my_o & -mx_o & 0 \\ 0 & -mz_o & my_o & I_{XX} & -I_{XY} & -I_{XZ} \\ mz_o & 0 & -mx_o & -I_{YX} & I_{YY} & -I_{YZ} \\ -my_o & mx_o & 0 & -I_{ZX} & -I_{ZY} & I_{ZZ} \end{bmatrix} \quad (3)$$

$$\vec{\tilde{f}} = [\tilde{M}_S]\vec{\ddot{\tilde{x}}} \tag{4}$$

$$\begin{bmatrix} \vec{\hat{f}}_1 \\ \vec{\hat{f}}_2 \\ \vdots \\ \vec{\hat{f}}_N \end{bmatrix} = \begin{bmatrix} [\hat{M}_1] & [0] & \cdots & [0] \\ [0] & [\hat{M}_2] & \cdots & [0] \\ \vdots & \vdots & \ddots & \vdots \\ [0] & [0] & \cdots & [\hat{M}_N] \end{bmatrix} \begin{bmatrix} \vec{\ddot{\hat{x}}}_1 \\ \vec{\ddot{\hat{x}}}_2 \\ \vdots \\ \vec{\ddot{\hat{x}}}_N \end{bmatrix} \tag{5}$$

The $[\tilde{K}_S]$ is calculated as the inverse of the compliance matrix $[\tilde{C}_S]$ as seen in Eq. (6), therefore the method revolves primarily around the extraction of the latter; this choice is made to facilitate the formulation of $[\tilde{K}_S]$ in terms of the reference nodes. This is done by treating the columns of $[\tilde{C}_S]$ as unit shapes $\vec{\tilde{c}}_j$, where each $\vec{\tilde{c}}_j$ corresponds to the displacement vector resulting from the application of a unit load f_j at a single DoF $j = \{1, 2, \ldots, Q\}$, where Q is the total number of DoF (in this case 277). Ultimately, the structure's displacement $\vec{\tilde{x}}$ under an applied load case $\vec{\tilde{f}}$ can be interpreted as the superposition of these unit shapes, scaled by the corresponding load component; this is shown in Eq. (7). Through the RBE3, it is possible to apply static loads and extract displacement on the reference nodes of interest in the FE model. The $[\tilde{C}_S]$ is therefore assembled one column at a time, by running a total of Q subcases, each time applying a single f_j and extracting the corresponding $\vec{\tilde{c}}_j$.

$$\vec{\tilde{f}} = [\tilde{K}_S]\vec{\tilde{x}} \leftrightarrow \vec{\tilde{x}} = [\tilde{C}_S]\vec{\tilde{f}} \tag{6}$$

$$\vec{\tilde{x}} = [\vec{\tilde{c}}_1 \vec{\tilde{c}}_2 \cdots \vec{\tilde{c}}_Q] \begin{bmatrix} f_1 \\ f_2 \\ \vdots \\ f_Q \end{bmatrix} = \sum_{j=1}^{Q} \vec{\tilde{c}}_j f_j \tag{7}$$

The method described above is best suited for structures under static equilibrium, where applied loads result in elastic deformation $\vec{\tilde{x}}^{EL}$. In the 2BTH system, the unconstrained rotation of the skewed hinge causes the shape to be a combination of $\vec{\tilde{x}}^{EL}$ as well as rigid body rotation along the hinge axis $\vec{\tilde{x}}^{RB}$. However, the unconstrained DoF at the hinge does not allow the moments to balance when a static load is applied, prohibiting the extraction of the $\vec{\tilde{c}}_j$. Therefore, the $[\tilde{C}_S]$ is calculated in two steps, as the sum of the compliance matrix due to elastic deformation $[\tilde{C}_S^{EL}]$ and rigid body rotation $[\tilde{C}_S^{RB}]$. In the case of $[\tilde{C}_S^{EL}]$, clamped boundary conditions are applied at the hinge node, resulting in unit shapes due to elastic deformation $\vec{\tilde{c}}_j^{EL}$. The calculation of $[\tilde{C}_S^{RB}]$ requires the introduction of a soft spring, to oppose rotation along the hinge axis, thereby imparting static equilibrium. The f_j are transformed to the equivalent moments along the hinge axis and applied to the structure, such that the resulting rigid body unit shapes $\vec{\tilde{c}}_j^{RB}$ are free of elastic deformation.

It must be noted that the spring's stiffness needs to be low enough, such that its effects are negligible in the EoM after the introduction of rotordynamic and aerodynamic terms. In principle, it is possible to extract the $[\tilde{C}_S]$ using the unit shapes featuring combined elastic and rigid body displacement, however it was found that for very low spring stiffness, the resulting $\vec{\tilde{c}}_j$ were dominated by rigid body displacement, losing precision in the component of elastic displacement. Likewise, an adequate increase in spring stiffness was found to affect the dynamics of the system, no longer being dominated by other terms in the EoM.

The ROM is validated against the FE model through an eigenvalue analysis. The two sets of modal frequencies f^{FE}, f^{ROM} are shown in Table 1. The labels "F", "E" and "TO" indicate flapwise bending, edgewise bending and torsion modes. Equivalently, the labels "S" and "A" correspond to symmetric and antisymmetric modes respectively; these mode pairs arise in flapwise modes due to the presence of the unconstrained hinge, the latter featuring rigid body displacement. The percentage offset is calculated, using f^{FE} as reference. The first 9 modes exhibit beam-like behaviour (flapwise, edgewise, torsion) and are therefore considered in the comparison. The first mode is a Rigid Body Motion (RBM) mode corresponding to unconstrained motion along the skewed hinge. From mode 10 onwards, the modeshapes are increasingly characterised by local deformations on the compliant parts of the cross section and can no longer be classified as beam modeshapes. Such higher modeshapes cannot be captured by the ROM accurately, however,

a good match is observed for the first 9 modes, as shown by the offset between f^{FE} and f^{ROM}, which is maintained within 2.5% error.

Table 1 Natural frequencies for the FE-ROM models

Mode Description	f^{FE} [Hz]	f^{ROM} [Hz]	Error [%]
Mode 1 - RBM	0.0302	0.0302	0.00
Mode 2 - F1S	3.6936	3.6754	-0.49
Mode 3 - F1A	7.4939	7.5169	0.31
Mode 4 - E1	8.1571	8.1581	0.01
Mode 5 - F2S	12.0058	11.7739	-1.93
Mode 6 - F2A	17.4619	17.3448	-0.67
Mode 7 - TO1	22.5884	22.9208	1.47
Mode 8 - F3S	23.4722	23.3061	-0.71
Mode 9 - E2	27.8533	27.1713	-2.45

3. Rotordynamics

Having validated the ROM, the lumped parameter approximation is used to model rotordynamics. Analytical expressions for the reduced order centrifugal stiffness matrix $[\tilde{K}_{CE}]$ and Coriolis damping matrix $[\tilde{B}_{CO}]$ are derived based on the segment's $[\hat{M}_i]$ in a RFR of constant Ω along the z-axis. Similar to the assembly of $[\tilde{M}_S]$ using a series of $[\hat{M}_i]$, the $[\tilde{K}_{CE}]$ and $[\tilde{B}_{CO}]$ are assembled using 6-by-6 matrices $[\hat{K}_{CE,i}]$, $[\hat{B}_{CO,i}]$, which capture the rotordynamics of a blade segment in isolation. The two analytical expressions are derived from the segment's $[\hat{M}_i]$, as shown in Eq. (8) and (9), representing the rotordynamics of arbitrarily shaped, unbalanced structures, such as the blade segments.

$$[\hat{K}_{CE,i}] = -\Omega^2 \begin{bmatrix} m & 0 & 0 & 0 & mz_o & -my_o \\ 0 & m & 0 & -mz_o & 0 & mx_o \\ 0 & 0 & 0 & 0 & 0 & 0 \\ 0 & -mz_o & 0 & I_{YY} - I_{ZZ} & 0 & -I_{XZ} \\ mz_o & 0 & 0 & 0 & I_{XX} - I_{ZZ} & -I_{YZ} \\ -my_o & mx_o & 0 & -I_{ZX} & -I_{ZY} & 0 \end{bmatrix} \tag{8}$$

$$[\hat{B}_{CO,i}] = -2\Omega \begin{bmatrix} 0 & m & 0 & -mz_o & 0 & mx_o \\ -m & 0 & 0 & 0 & -mz_o & my_o \\ 0 & 0 & 0 & 0 & 0 & 0 \\ mz_o & 0 & 0 & 0 & -(I_{ZZ} - I_{XX} - I_{YY})/2 & -I_{YZ} \\ 0 & mz_o & 0 & -(I_{ZZ} - I_{XX} - I_{YY})/2 & 0 & I_{XZ} \\ -mx_o & -my_o & 0 & I_{ZY} & -I_{ZX} & 0 \end{bmatrix} \tag{9}$$

A numerical experiment is carried out in MSC Nastran to validate the derived expressions for $[\tilde{K}_{CE}]$ and $[\tilde{B}_{CO}]$. This is done by comparing the following two methods in parallel:

1) Reference: Complex eigenvalue analysis (SOL107) using the "Rotordynamics" package to define the RFR and range of Ω in the AUX model.
2) Analytical: Complex eigenvalue analysis (SOL107) where the analytical expressions for $[\hat{K}_{CE,i}]$ and $[\hat{B}_{CO,i}]$ are supplied to the AUX model as "Direct Matrix Input" to the reference nodes, using DMIG entries.

The purpose of the numerical experiment is to isolate and assess the effect of $[\tilde{K}_{CE}]$ and $[\tilde{B}_{CO}]$ on the EoM. On that note, the FS rotor's relatively high stiffness and low inertia were found to complicate the validation of the analytical expressions, as the $[\tilde{K}_{CE}]$ and $[\tilde{B}_{CO}]$ were found to have a minimal effect on the EoM at the intended range of Ω, $\Omega = 1.53$Hz being the design speed set by the project partners. Therefore, an auxiliary model (AUX) is constructed for validation purposes, emulating the FS rotor in terms of being a line beam simply supported by a skewed hinge at mid-span. The AUX rotor is less stiff and has increased inertia, imparted through the addition of concentrated mass elements (CONM2); the latter are also used to emulate the imbalance of the blade segment, by introducing offsets $\{x_o, y_o, z_o\}$ between the reference node and the CoG. Finally, structural damping of $\zeta = 0.5\%$ is also included.

A Campbell diagram is shown in Fig. 5 comparing the two methods, which are found to match closely, hence validating the derived analytical expressions. Interestingly, with the exception of the edgewise mode which becomes overdamped, the remaining modes remain mostly unaffected. Given the reduced significance of the edgewise mode in the context of a low fidelity aeroelastic system, $[\tilde{K}_{CE}]$ and $[\tilde{B}_{CO}]$ could be omitted from the EoM for studies on a similar system.

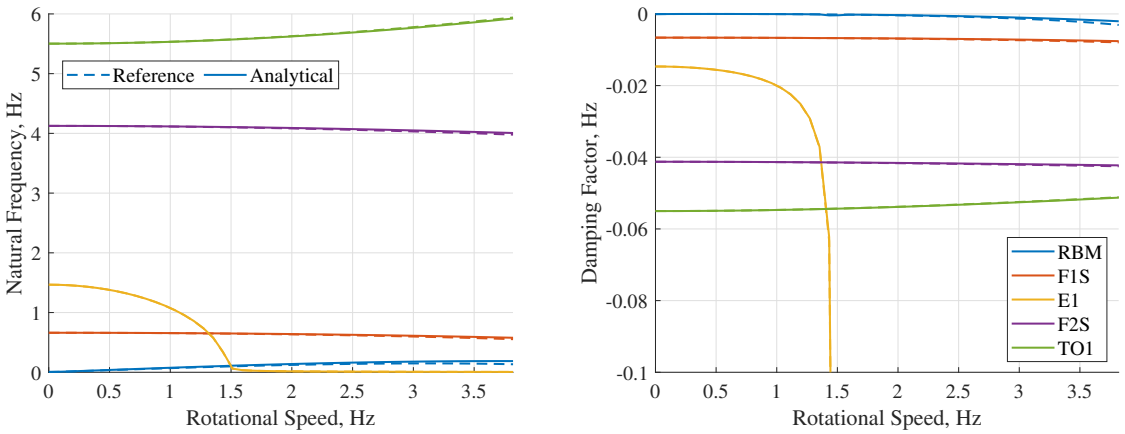

Figure 5 Validation of rotordynamics modelling

4. Geometric Stiffness

Geometric stiffness accounts for the displacement of nodes and points of force application as a result of deformation; their respective relocation in space leads to the formation of previously non-existent moment arms, ultimately introducing moments proportional to $\vec{x}$ in the EoM. This is illustrated in Fig. 6, where a constant axial force is applied to a simply supported deformed structure, leading to a spanwise bending moment distribution M_X. In their work, Shah and Pilkey [14] and Senjanovic et al. [15] present expressions for the lumped geometric stiffness matrix, as a result of an applied axial force. In the former case, the moments are lumped at the rotational DoF, with the advantage of yielding symmetric matrices. In the latter, the differences in the translational DoF are utilised instead; this is a more accurate representation of the underlying physics, as this phenomenon is driven by node translation, whereas the use of the rotational DoF is a simplification valid for negligible curvature between nodes.

In the proposed approach, M_X is recreated by splitting the structure into spanwise segments, such that the axial load is applied on the outboard node and M_X is calculated on the inboard node. The calculated M_X is applied on both nodes as $M_X/2$ and propagates towards the root of the structure, as illutrated in Fig. 6; a model of a simply supported beam is used, split into four spanwise segments and loaded axially at the end of the fourth and last segment by a force f_Y^4. The sum of the applied M_X from each segment approximates the total M_X distribution. The beam combines rigid body rotation at the root with elastic displacement.

The ROM geometric stiffness $[\tilde{K}_{GE}]$ is assembled from the matrices $[\hat{K}^j_{GE,i}]$ corresponding to each spanwise segment i, for each applied load f_Y^j, where $j \geq i$, as shown in Eq. (10) and Eq. (11); note that it is not necessary for all nodes on the structure to be subjected to a load f_Y^j. In the context of a blade, for each f_Y^j, a geometric stiffness matrix $[\hat{K}^j_{GE}]$ is calculated by adding the $[\hat{K}^j_{GE,i}]$, starting from the node of force application and moving towards the root.

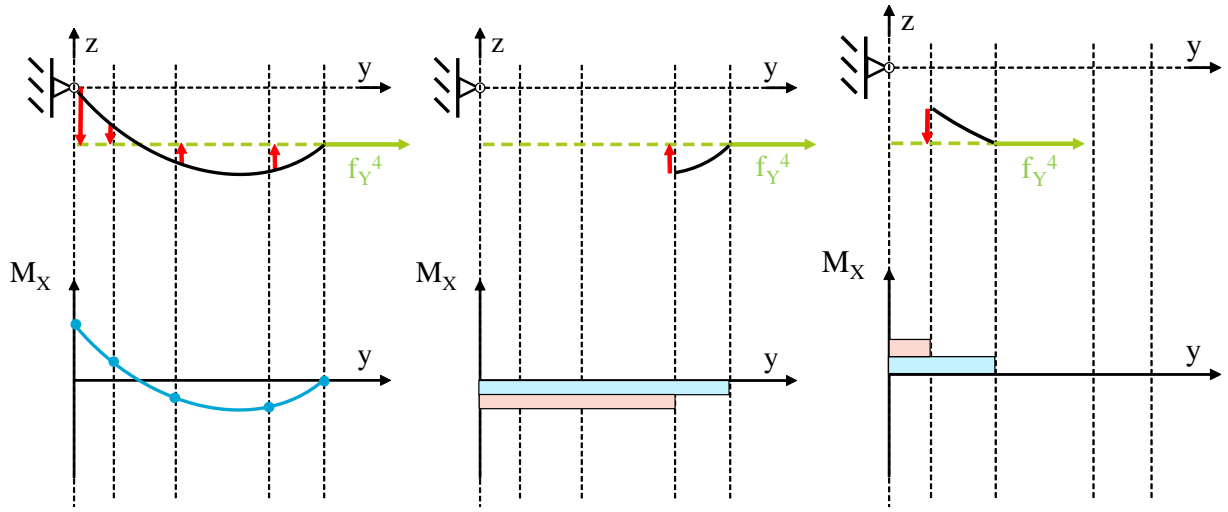

Figure 6 Proposed approximation of M_X due to applied axial load on a deformed structure

This is repeated for all applied forces to finally calculate $[\tilde{K}_{GE}]$. An analytical expression for $[\hat{K}^j_{GE,i}]$ is defined, as shown in Eq. (12), relating the relevant translational DoF $(\tilde{x}, \tilde{z})$ to the moments at nodes i and $i-1$.

$$[\tilde{K}_{GE}] = \sum_{j=1} [\hat{K}^j_{GE}] \tag{10}$$

$$[\hat{K}^j_{GE}] = \sum_{i=1}^{j} [\hat{K}^j_{GE,i}] \tag{11}$$

$$\begin{bmatrix} M_{X,i-1} \\ M_{Z,i-1} \\ M_{X,i} \\ M_{Z,i} \end{bmatrix} = [\hat{K}^j_{GE,i}] \begin{bmatrix} \tilde{x}_{i-1} \\ \tilde{z}_{i-1} \\ \tilde{x}_i \\ \tilde{z}_i \end{bmatrix} = -f^j_Y/2 \begin{bmatrix} 0 & 1 & 0 & -1 \\ -1 & 0 & 1 & 0 \\ 0 & 1 & 0 & -1 \\ -1 & 0 & 1 & 0 \end{bmatrix} \begin{bmatrix} \tilde{x}_{i-1} \\ \tilde{z}_{i-1} \\ \tilde{x}_i \\ \tilde{z}_i \end{bmatrix} \tag{12}$$

Similar to the rotordynamic expressions, the analytical expression for $[\tilde{K}_{GE}]$ is validated via a numerical experiment in MSC Nastran; the same AUX model is used to facilitate the comparison between rotordynamics and geometric stiffness, in terms of their relative influence on the EoM. The following two methods are compared:

1) Reference: Complex eigenvalue analysis (SOL107), where geometric stiffness is introduced to the AUX model using a pair of subcases; the first is used to define the applied force and is referenced by the second using STATSUB, which then performs the complex eigenvalue analysis.
2) Analytical: Complex eigenvalue analysis (SOL107), where the analytical expression for $[\tilde{K}_{GE}]$ is supplied to the AUX model as "Direct Matrix Input" to the reference nodes, using DMIG entries.

The results of the numerical experiment are shown in a Campbell diagram in Fig. 7, indicating good agreement between the two methods. It must be noted that the $[\tilde{K}_{GE}]$ has a more significant effect on the system's vibration behaviour than the $[\tilde{K}_{CE}]$, $[\tilde{B}_{CO}]$, causing significant stiffening in the rigid body, flapwise and edgewise modes over the same range of Ω.

The proposed formulation can also be extended to account for the geometric stiffening effects due to the application of normal forces f^j_X, f^j_Z, on a deformed structure. The expressions for the corresponding $[\hat{K}^j_{GE,i}]$ have been derived based on the same principles of formation of moment arms due to displacement of the points of force application. However, the analytical expressions could not be validated using the above numerical experiment, therefore the presented analysis and results only consider f^j_Y, in the calculation of $[\tilde{K}_{GE}]$.

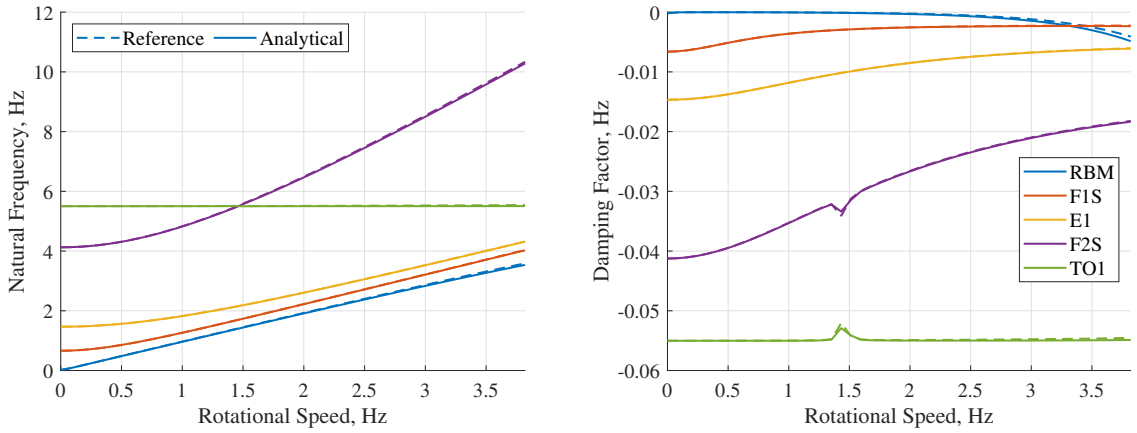

Figure 7 Validation of geometric stiffness modelling

III. Wind Tunnel-Scale Rotor Design

A. Scaling Methodology

1. Non-Dimensional Parameters

Full-scale physical systems are scaled in accordance with the "Buckingham Π-theorem", which states that the scaled model and the reference FS model exhibit the same behaviour if all the non-dimensional parameters Π_i resulting from the terms of the governing equations are matched [16]. In practice, it is well understood that it is often impossible to match all the parameters, due to practical limitations.; this is the case with the Reynolds number Re, shown in Eq. (13), where ρ is the density of air, W is section airspeed, c is section chord and μ is the dynamic viscosity of air. In wind turbines, a decrease in length scale causes a quadratic decrease in Re. For conventional wind tunnels, where ρ and μ cannot be altered, this could only be overcome by an equivalent increase in W and Ω, which is typically not possible in practice. Therefore, WT testing of downscaled wind turbines is inherently limited by the unavoidable Re mismatch.

$$Re = \rho W c/\mu \tag{13}$$

In addition, it is possible that the FS and WT model have no sensitivity to some of the Π_i which arise from the above analysis for the intended operational envelope; such examples include the Mach number Ma and the Froude number Fr, shown in Eq. (14) and (15) respectively, where α_S is the speed of sound in air and g is gravitational acceleration. In the case of the former, values below $Ma = 0.3$ are anticipated in both the FS and WT models, where the effects of flow compressibility are negligible. Regarding the latter, the FS model has a diameter of 30m, at which length scale the effects of gravitational loads are considered negligible; this also applies to the WT model.

$$Ma = W/\alpha_S \tag{14}$$

$$Fr = V^2/gR \tag{15}$$

The design of the scaled rotor and WT testing campaign revolves around matching the remaining, attainable parameters. In their work, Canet et al. [9] summarise the main parameters pertinent to aeroelastic wind tunnel testing of wind turbines. The identified parameters are presented in Table 2, where R is the rotor radius, C_L is the coefficient of lift, C_D is the coefficient of drag, T is the aerodynamic thrust force, Q is the aerodynamic torque along the rotor axis and n is the mode number. The parameters are categorised based on their relation to aerodynamics, structural design or both.

The first few Π_i are focused on matching the system's aerodynamics. Maintaining the same normalised rotor planform, in terms of airfoil, chord and pre-twist distribution ensures geometric similarity. The tip speed ratio λ determines the velocity triangle and wake helix pitch. The normalised circulation $\bar{\bar{\Gamma}}$ characterizes rotational augmentation due to spanwise flow as well as wake behaviour. The thrust coefficient C_T, which is mainly a function of C_L, is used

Table 2 Attainable Π_i for wind turbine scaling

Description	Mathematical Expression	Aero.	Struc.
Normalised rotor planform	-	✓	
Tip speed ratio	$\lambda = R\Omega/V$	✓	
Normalised circulation	$\bar{\bar{\Gamma}} = cC_L/2R$	✓	
Thrust coefficient	$C_T = T(C_L)/1/2\rho V^2\pi R^2$	✓	
Power coefficient	$C_P = Q(C_L, C_D)/1/2\rho V^3\pi R^2$	✓	
Lock number	$Lo = C_L\rho cR^4/I_{XX}$	✓	✓
Reduced frequencies	$k_n = \omega_n c/2W$	✓	✓
Normalised natural frequencies	$\bar{\bar{\omega}}_n = \omega_n/\Omega$		✓
Normalised modeshapes	$\vec{\bar{\bar{\phi}}}_n$		✓
Normalised static displacement	$\vec{\bar{\bar{x}}}$		✓

to capture the wake deficit and the aerodynamic loads on the rotor. Finally, the power coefficient C_P, which is a function of both C_L and C_D, represents the efficiency of the rotor in terms of converting wind energy to mechanical energy. Before moving on to the structural Π_i, the following two parameters combine aerodynamic and structural effects. First, the Lock number Lo captures the ratio of aerodynamic-to-inertial loads. Second, the reduced frequencies k_n govern the magnitude and phase of the aerodynamic response of an airfoil in harmonic motion. The remaining three parameters revolve around the rotor's structural characteristics. Starting with normalised natural frequencies $\bar{\bar{\omega}}_n$ and normalised modeshapes $\vec{\bar{\bar{\phi}}}_n$, these parameters determine the vibration behaviour. Finally, matching the normalised static displacement $\vec{\bar{\bar{x}}}$, under the application of the same normalised load, captures the structure's stiffness.

2. Strategy

In the context of this study, two boundary conditions are enforced. The first regards the choice of wind tunnel, with the Open Jet Facility (OJF) WT of Delft University of Technology being chosen for the planned wind tunnel campaign. Consequently, the FS rotor is downscaled from a diameter of 30m to 1.2m, to comply with the size limitations of the WT; this corresponds to a length scaling factor $n_L = 25$. Accordingly, the maximum possible generated wind speed is 30m/s. The second boundary condition is associated with the decision to reuse the existing testing equipment, including the rotor hub, previously built and instrumented by the project partners for a 1.2m diameter demonstrator rotor. Therefore, Ω =750RPM=12.5Hz is set as an upper limit, to ensure safe and robust operation. The design of the WT scale rotor and testing campaign revolves around these boundary conditions and focuses solely on the design of the blades, in accordance with the Π_i identified in Section III.A.1. The blade design is the result of a two-step optimisation, focusing on aerodynamics and structural design separately, as shown below. Matching these characteristics individually ultimately corresponds to matching the aeroelastic properties of the system.

The aim of the aerodynamic optimisation is to match the identified aerodynamic Π_i as closely as possible. Upon inspection of the expressions on Table 2, this is partly achieved by enforcing the same normalised rotor planform, in terms of the spanwise chord and twist distribution, as well as λ. Having established the above, the objective of the aerodynamic optimisation is to mitigate the effects of the Re mismatch in terms of C_L and C_D, so as to minimise the deviation in $\bar{\bar{\Gamma}}$, C_T, C_P as well as Lo. This is done in two ways. First, a high enough W is ensured, by constraining rotational speed to a minimum allowable Ω = 450RPM = 7.5Hz; this would result to a $Re = 1.1 \cdot 10^5$ at 75%-span, well above the threshold of $Re = 7.0 \cdot 10^4$, below which smooth airfoils exhibit poor aerodynamic performance [17]. For reference, the FS model experiences a value of $Re = 1.4 \cdot 10^7$ at 75%-span, for Ω = 91.67RPM = 1.53Hz. Second, geometric similarity is overlooked, in favour of aerodynamic performance, by switching airfoils. The original NACA63618 airfoil was found to perform poorly in the intended low Re range, hence it was decided to replace it with an airfoil whose C_L, C_D, as well as the coefficient of moment about the aerodynamic centre C_M match the FS model at $Re = 1.4 \cdot 10^7$. The airfoil of choice is the SD7062 which combines good aerodynamic performance at low Re with a relatively large maximum thickness-to-chord ratio $t/c = 14\%$; maximising the latter also facilitates matching structural properties as well as fitting sensors in the limited allowable space, especially at the blade tip. Fig. 8 compares the two airfoils at low Re, relative

to the target aerodynamic polars; the data is generated using XFOIL [18]. It is evident from the three graphs that the SD7062 airfoil improves the match in C_L, C_D and C_M at low Re, matching the C_L at $Re > 10^5$ whilst reducing the inevitable mismatch in C_D. The former corresponds to a match in $\bar{\bar{\Gamma}}$ and C_T, as well as the aerodynamic component of Lo, whereas the latter alleviates the deviation in C_P. Finally, transition strips are applied at $5\% - c$, as they were found to be effective in mitigating the effects of flow separation at low Re [8].

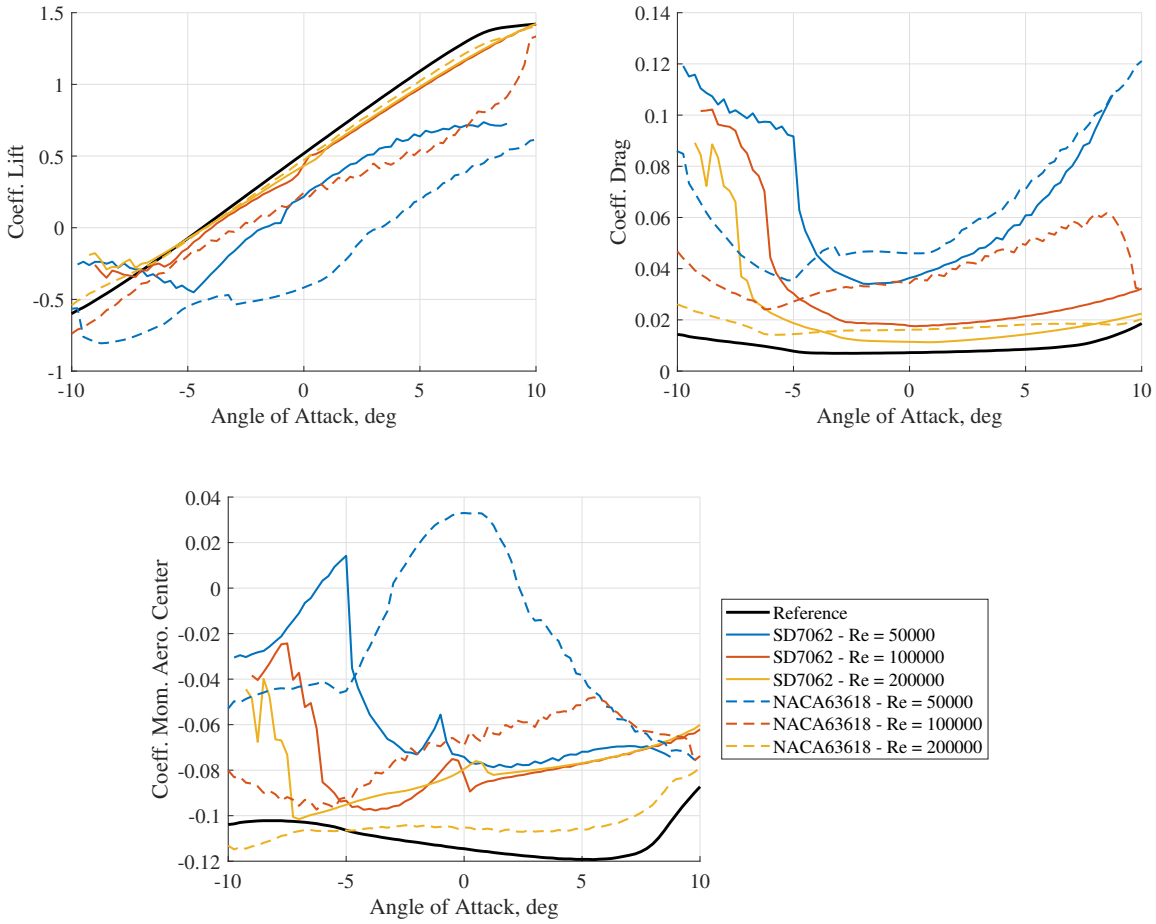

Figure 8 Airfoil polars of SD7062, NACA63618 at low Re

The structural optimisation in principle targets the WT model's $[K_S]$ and $[M_S]$. Therefore, a FE model of the rotor is generated in MSC Nastran, including the hub provided by the project partners, such that the blades are subjected to design optimisation, using the Design Sensitivity & Optimisation package (SOL200); the MSC Nastran optimisation methodology is described in detail in Section III.C. In the above list of Π_i, the parameters of interest are Lo, $\bar{\bar{\omega}}_n$, k_n, $\vec{\bar{\bar{\phi}}}_n$ and $\vec{\bar{\bar{x}}}$. Provided that λ is matched, as well as the normalised chord profile, matching $\bar{\bar{\omega}}_n$ guarantees also matching k_n. Upon inspection using the FE model, it was found that the I_{XX} foreseen by Lo, would be impossible to match due to manufacturability constraints on the minimum allowable feature thicknesses at such small scale. Furthermore, the use of the existing hub, which was not designed according to scaling laws, adds unrealistically high inertia to the system, further complicating the design of a Lo-scaled rotor. A mismatch in Lo, and therefore $[M_S]$, automatically prohibits the simultaneous matching of $\bar{\bar{\omega}}_n$, $\vec{\bar{\bar{\phi}}}_n$ and $\vec{\bar{\bar{x}}}$. This is because the former two depend on $[K_S]/[M_S]$ whereas the latter only depends on $[K_S]$. Hence, it was decided to produce two designs: a "stiff" rotor, which compensates for the increased $[M_S]$ by increasing $[K_S]$ accordingly, and a "flexible" rotor, which matches $[K_S]$ at the expense of vibration behaviour. Therefore, the former targets the $\bar{\bar{\omega}}_n$, $\vec{\bar{\bar{\phi}}}_n$ and will be used to assess the vibration behaviour of the system. Likewise, the

latter targets $\vec{\bar{x}}$ by scaling a static aerodynamic load case appropriately and will be used to assess the static aeroelastic behaviour of the system. Upon inspection, it was decided to conduct the WT tests at Ω = 600RPM = 10Hz, as higher Ω compromised the optimiser's ability to match $\bar{\omega_n}$, whilst causing the resulting designs to be heavier and deviate further from the target Lo.

B. Blade Design Templates

Having established that two separate rotors will be tested, two design templates are developed; the templates offer a generalised description of a spanwise segment, with the purpose of parametrisation for optimisation. Each template is tailored to facilitate matching the relevant structural properties. The aim for both templates is to be simple and cheap to produce and assemble, reducing the costs associated with prototype development. Therefore, a requirement is set for both blade templates to be 3D-printable as a single part, which is possible at this length scale (maximum dimension 0.48m). Specifically, the blades are meant to be produced using the method of selective laser sintering, which is commercially available at low cost. This method of 3D-printing yields isotropic material properties and is compatible with polyamide-12, whose combination of low stiffness (1.65GPa), high strength (42-48MPa) and low density (930kg/m^3) enables the design of flexible, robust, lightweight structures. Another advantage of 3D-printing is its high tailoring potential in terms of feature sizing, provided that manufacturability guidelines are satisfied. Both templates describe the blade in terms of its cross-section, as seen in Fig. 9. In practice, the blades are split into a number of spanwise segments which are further split into chordwise partitions of constant thickness. With the addition of rib thickness, this amounts to 13 regions for the stiff blades and 6 regions for the flexible blades, indicated in grey in the template illustrations. These thickness values are the optimisation variables, constrained to a minimum allowable thickness of 1.2mm for shell partitions and 2mm for shear web and rib partitions, in accordance with guidelines from the manufacturer.

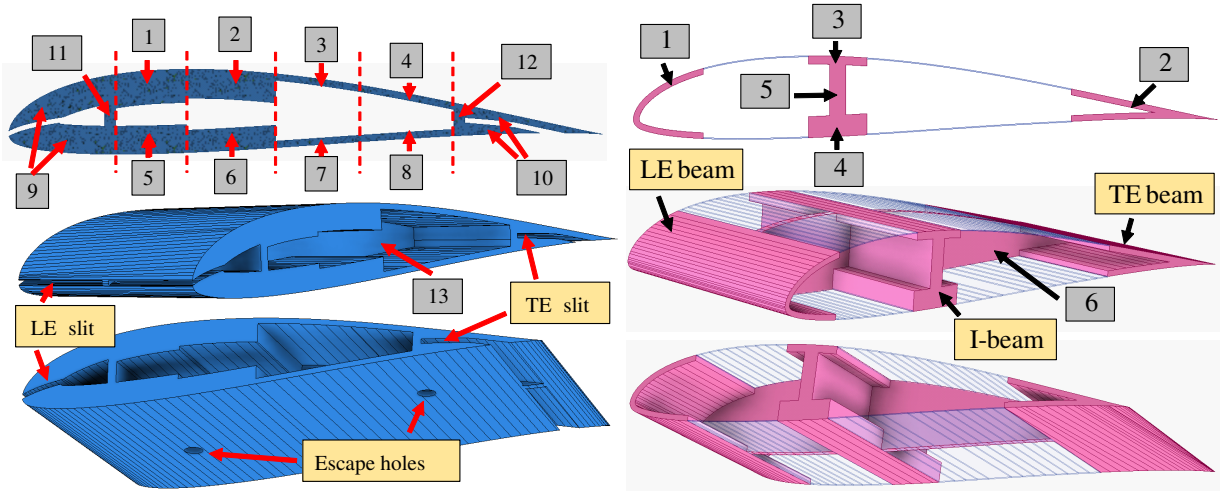

(a) Stiff blade segment **(b) Flexible blade segment**

Figure 9 The two blade design templates

The stiff blade aims to match $\bar{\omega_n}$ by maintaining the ratio with respect to Ω and by extension the ratio between the natural frequencies. This is achieved through a design featuring a closed cross-section with structural mass along its periphery; this distribution of mass leads to an increase in all natural frequencies. The ratio between frequencies can be challenging to meet, as individual modes are not decoupled from the others. In the context of this study, it was found that a closed section has a relatively higher torsional-to-flapwise stiffness ratio, than the reference FS model. This is mitigated by introducing slits along the leading and trailing edge. This adaptation effectively opens the LE and TE cell, which causes a significant decrease in torsional stiffness, at minimal decrease in flapwise stiffness. The width of the effective torsion box is adapted by adjusting the position of the two shear webs – in this case, they are positioned at 18%-c and 75%-c. The spanwise segment also features a rib at mid-span, with the purpose of shear support and stiffening of the LE and TE shell, minimising the possibility of warping associated with 3D-printing of

slender structures, at little added mass. In addition, "escape holes" are required when 3D-printing hollow parts with this method, to remove excess material during post-processing, which would otherwise be trapped. Therefore a pair of escape holes are featured, close to the corners formed by the ribs and the shear webs. The gaps introduced by the slits and escape holes are covered by applying a layer of Oralight foil [19], maintaining the outer airfoil geometry.

The flexible blade aims to match $\vec{\vec{x}}$. Recreating the same displacement profile at such smaller scale requires a highly flexible structure. This was found to be impossible with a closed cross-section structure, given the minimum allowable thickness constraint. Instead, a template was developed based on the work of Avin et al. [20]. The design features three slender beams (LE, middle, TE) which cover the entire span of the blade, joined by ribs. In the original design the LE and TE beams along with the ribs help guide the Oralight foil, to maintain the aerodynamic shape of the airfoil. The ribs also feature horizontal slits near mid-chord for a "stiffener plate" to pass through, made of aluminium, which tailors the structural properties of the wing. The template developed in the present study replaces the stiffener plate with an I-beam at $35\% - c$. It was found that this design could match $\vec{\vec{x}}$ at relatively low mass, whilst being 3D-printable as a single part, avoiding the cost and complexity associated with manufacturing and assembling the stiffener plate. The flanges of the I-beam also facilitate the application of the Oralight foil, offering an additional surface for adhesion.

C. Blade Design Optimisation

1. Optimisation Framework

The MATLAB-to-MSC Nastran toolchain described in Section II is also used for generating the FE models of the WT scale blades, shown in Fig. 10. All features are modelled using 2D elements; CTRIA3 for the shells, flanges and Oralight foil and CQUAD4 for the shear webs and ribs. A total of 10 spanwise segments make up the blade, each featuring a RBE3 element on its rib, along the y-axis. The segments at the root and tip have half the spanwise length and their ribs positioned at the corresponding end. The hub is split into 3 spanwise segments and 7 chordwise partitions and modelled using CQUAD4. The FE model was found to exhibit little sensitivity to changes in the hub, so a simplified representation is used, approximating it as a single aluminium plate. The exact geometry of the hub is approximated by tailoring the thickness and vertical offset of each partition, as shown in Fig. 10c. The hub is connected to the blade via RBE2 elements. In the centre of the hub, the skewed hinge connection is recreated by defining an additional node using the H coordinate system and connecting it to the nearest nodes on the hub using a RBE2. Finally, the integrated accelerometers and strain gauges are modelled as non-structural masses using CONM2 elements in the corresponding locations.

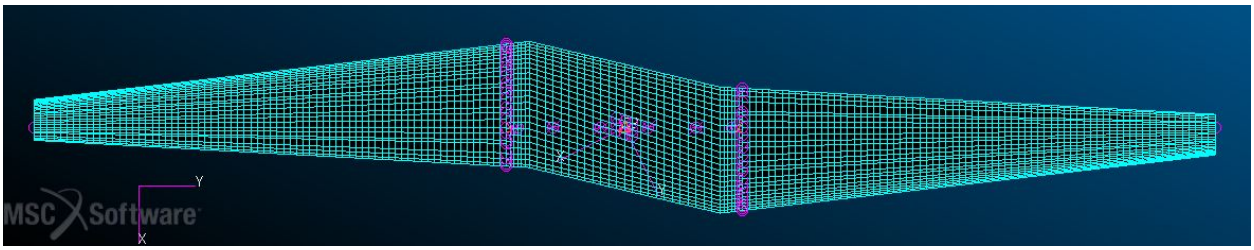

(a) Shell element model of rotor

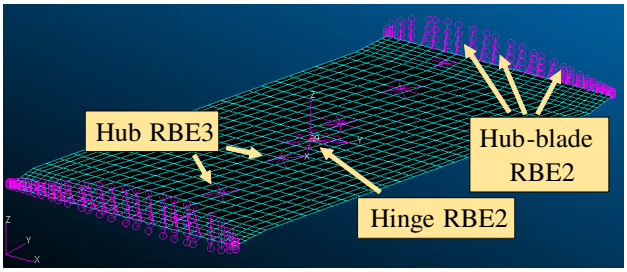

(b) CQUAD4 model of hub

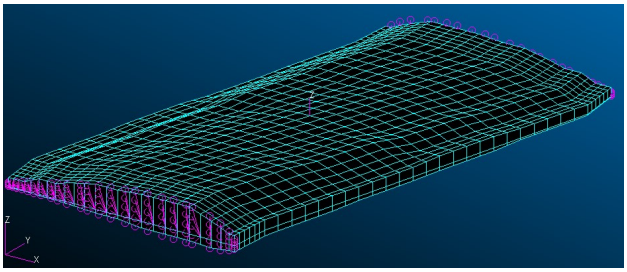

(c) 3D representation of hub geometry

Figure 10 MSC Nastran model of the WT-scale rotor

The first step towards defining optimisation strategies for the respective rotors is a parametric sensitivity study using

the FE models. In this context, the blades' thickness distributions were used to investigate the two templates' tailoring potential, as well as their limitations, in terms of matching the identified Π_i of interest. In both cases, structural integrity is guaranteed from the imposed minimum allowable thickness requirement, therefore strength and buckling constraints are omitted from the optimisation, making it more computationally efficient; instead, structural integrity is confirmed for the optimum design during post-processing, by scaling and applying the extreme load case provided by the project partners.

Regarding the stiff blade, it was found that the increased mass of the hub does not allow matching the S-A flapwise bending modes simultaneously, as anti-symmetric modes feature rigid body rotation of the hub along the hinge, causing them to have comparatively lower natural frequencies to their symmetric counterparts. Therefore it was decided to focus the stiff blade optimisation on matching the symmetric modes. In addition, edgewise modes proved impossible to match. This can be attributed to the combined effect of the following three reasons:

1) Change of airfoil: Switching airfoils, from 18% t/c to 14% t/c, causes a cubical reduction in the flapwise 2nd moment of area, as opposed to a linear reduction in the edgewise 2nd moment of area.
2) Hub geometry: There are significant differences in hub geometry between the FS and WT models. The former is approximated as a box-section beam of roughly 25%-c width located along the blade axis, whereas the latter is designed as a solid aluminium part spanning the entire root chord. The two models' difference in geometry is reflected in the edgewise 2nd moment of area, which is proportional to the cube of the width.
3) Stiffness distribution across the section: the FS design's shell is partitioned into regions of varying stiffness, the main girders imparting stiffness to the section, with the remaining shell made out PVC60 foam, mainly providing the desired airfoil shape. Ultimately, the section's stiffness results from the summed contribution of those regions' material and geometric properties. This effect is hard to reproduce with a single material, which is the case for the 3D-printed blades. Optimising the shell thickness along the section is the only tool available, however minimum allowable thickness constraints limit the tailoring potential. This is viewed as a drawback of building the blade as a single 3D-printed part.

In addition, the presence of the quasi-rigid hub was found to introduce a mismatch in the modeshapes, which remain undeformed until 20%-span; this error propagates to the whole span, causing an inevitable mismatch in $\bar{\bar{\phi}}_n$. Therefore, it was decided to omit the $\bar{\bar{\phi}}_n$ from the optimisation strategy. In contrast, the ability to match $\omega_{F1S}^{\bar{\bar{}}}$, $\omega_{F2S}^{\bar{\bar{}}}$ and $\omega_{TO1}^{\bar{\bar{}}}$ was confirmed by manually tuning the chordwise position of the shear webs, therefore it is imposed as an equality constraint. The objective function is formulated as the minimisation of $\omega_{E1}^{\bar{\bar{}}}$, which is inevitably significantly overestimated.

The optimisation of the flexible blades is exclusively based on matching $\bar{\bar{x}}$, with a focus on flapwise displacement $\Delta\bar{\bar{z}}$ and pitch $\Delta\bar{\bar{\theta}}$. An objective function f_{OBJ}^{FLEX} is formulated as the normalised root mean square (RMS) error of the blade's displacement profile, relative to the reference shape $\bar{\bar{x}}^{ref}$. The RMS error is multiplied by the rotor's I_{XX}, aiming to minimise the Lo mismatch, in the process of minimising f_{OBJ}^{FLEX}; f_{OBJ}^{FLEX} is shown in Eq. (16). An additional equality constraint requires $\Delta\bar{\bar{z}}_N$, $\Delta\bar{\bar{\theta}}_N$ at the blade tip (such that $i = N$) to match the reference values. It must be noted that the load case features the blade without the hub, under clamped boundary conditions at the root section; this adaptation is made to avoid complications due to differences between the full-scale and wind tunnel-scale models of the hub.

$$f_{OBJ}^{FLEX} = I_{XX}\sqrt{\sum_{i=1}^{N}\left(\left(\frac{\Delta\bar{\bar{z}}_i - \Delta\bar{\bar{z}}_i^{ref}}{\Delta\bar{\bar{z}}_i^{ref}}\right)^2 + \left(\frac{\Delta\bar{\bar{\theta}}_i - \Delta\bar{\bar{\theta}}_i^{ref}}{\Delta\bar{\bar{\theta}}_i^{ref}}\right)^2\right)} \tag{16}$$

2. Results

The optimisation results are presented below. The target inertia matrix $[I^{LO}]$ is determined from Lo, by dividing the FS inertia matrix by n_L^5, as the remaining terms in the expression (C_L, ϱ, c and R) are pre-defined. The inertia matrix of the hub $[I^{HUB}]$, stiff rotor $[I^{STIFF}]$ and flexible rotor $[I^{FLEX}]$ are also presented in Table 3. The $[I^{HUB}]$ is presented to demonstrate how the inclusion of the solid aluminium hub imparts inertia that exceeds the target values of $[I^{LO}]$ before the blades are even added to the structure. The Lo, which captures the ratio of aerodynamic to inertial forces, is relevant in the present context as the rotor features an unconstrained DoF along the skewed hinge and a relative increase in the latter is expected to affect the rigid body kinematics of hinge rotation. The sensitivity of rotor aerodynamics to rigid body kinematics was also reported by Krishnan et al. [10]. Interestingly, even though the flexible blades have

significantly reduced inertia compared to their stiff counterparts, a substantial mismatch in Lo remains.

Table 3 Inertia matrices

$[I^{LO}]\ [kgm^2]$			$[I^{HUB}]\ [kgm^2]$		
$1.17 \cdot 10^{-2}$	$-3.93 \cdot 10^{-4}$	0	$4.91 \cdot 10^{-3}$	$-7.81 \cdot 10^{-4}$	0
$-3.93 \cdot 10^{-4}$	$1.50 \cdot 10^{-4}$	0	$-7.81 \cdot 10^{-4}$	$1.23 \cdot 10^{-3}$	0
0	0	$1.18 \cdot 10^{-2}$	0	0	$6.13 \cdot 10^{-3}$
$[I^{STIFF}]\ [kgm^2]$			$[I^{FLEX}]\ [kgm^2]$		
$5.47 \cdot 10^{-2}$	$-1.54 \cdot 10^{-3}$	0	$2.91 \cdot 10^{-2}$	$-1.45 \cdot 10^{-3}$	0
$-1.54 \cdot 10^{-3}$	$1.66 \cdot 10^{-3}$	0	$-1.45 \cdot 10^{-3}$	$1.47 \cdot 10^{-3}$	0
0	0	$5.63 \cdot 10^{-2}$	0	0	$3.06 \cdot 10^{-2}$

Regarding the stiff rotor, Table 4 presents the natural frequencies resulting from the design optimisation $\bar{\bar{\omega}}_n$ compared to the target values derived from scaling laws $\bar{\bar{\omega}}_n^{ref}$. For the three modes of interest, a good match within ±2.7% error is obtained. As anticipated, $\bar{\bar{\omega}}_{E1}$ is significantly higher than the target value.

Table 4 Normalised natural frequencies

Mode Description	$\bar{\bar{\omega}}_n^{ref}[-]$	$\bar{\bar{\omega}}_n[-]$	Error [%]
F1S	2.42	2.35	-2.64
E1	5.34	13.10	145.45
F2S	7.85	7.72	-1.59
TO1	14.79	14.97	1.33

The obtained modeshapes $\vec{\bar{\bar{\phi}}}_{F1S}$, $\vec{\bar{\bar{\phi}}}_{F2S}$, $\vec{\bar{\bar{\phi}}}_{TO1}$ are shown in Fig. 11, 12, 13 respectively, in terms of $\Delta\bar{\bar{x}}$, $\Delta\bar{\bar{z}}$ and $\Delta\bar{\bar{\theta}}$. Each modeshape is normalised with respect to the maximum displacement component at the tip ($\vec{\bar{\bar{\phi}}}_{F1S}$, $\vec{\bar{\bar{\phi}}}_{F2S}$ - $\Delta\bar{\bar{z}}_N$, $\vec{\bar{\bar{\phi}}}_{TO1}$ - $\Delta\bar{\bar{\theta}}_N$). The influence of the increased stiffness of the WT hub is evident in all cases, as the displacement components on the hub nodes, found between the shaft and 20%-span, are almost zero; this observation validates the omission of modeshapes from the optimisation strategy. An adverse consequence of this simplification is the lack of bend-twist coupling in the WT blades, which is present in the FS model.

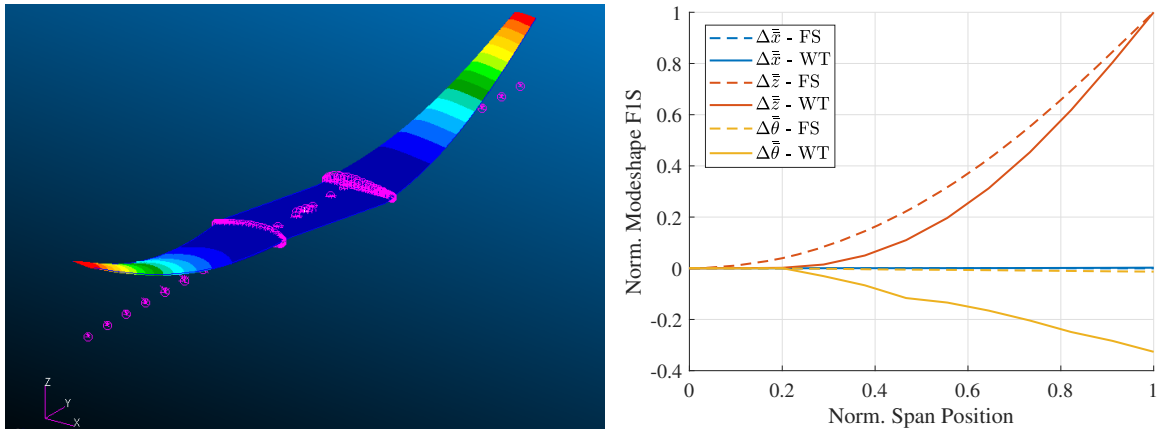

Figure 11 Modeshape F1S

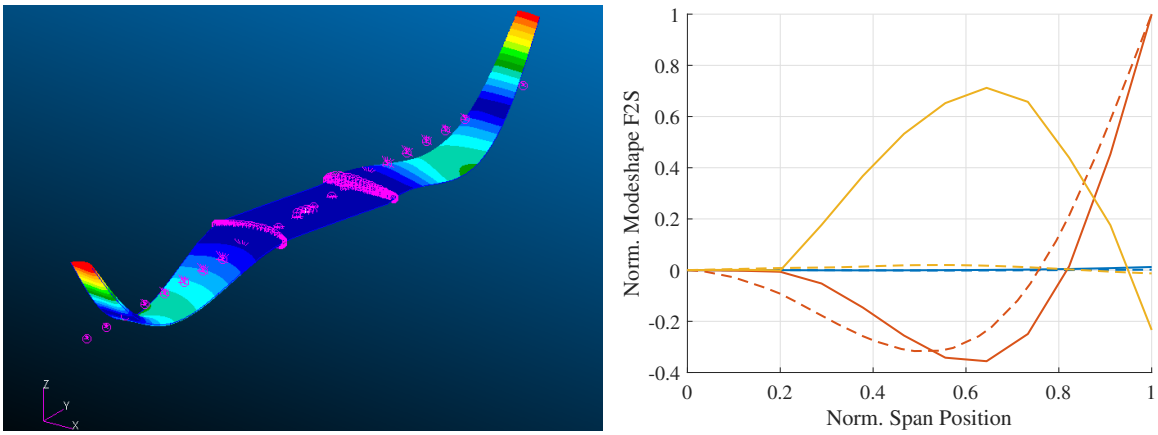

Figure 12 Modeshape F2S

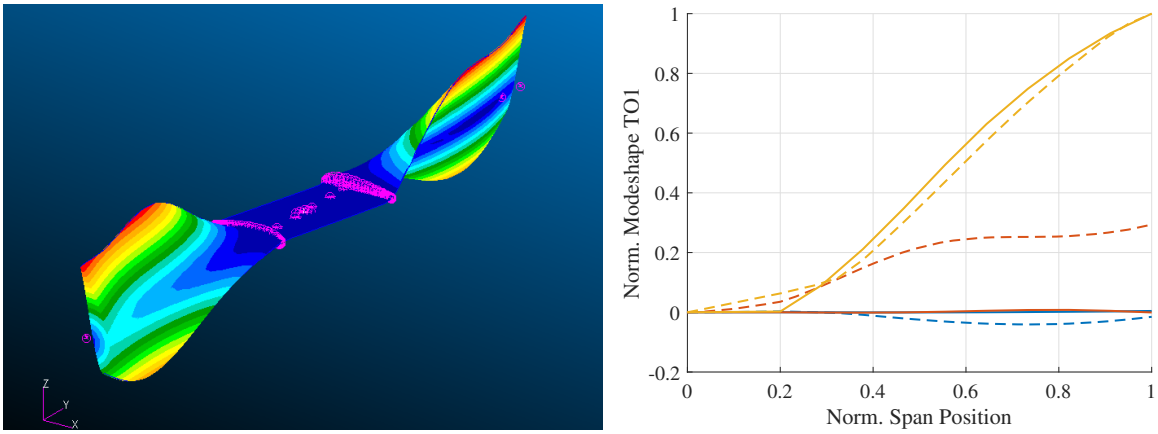

Figure 13 Modeshape TO1

The flexible rotor is optimised by focusing on the blades, irrespective of the hub. The normalised displacement profiles $\Delta\bar{\bar{z}}$, $\Delta\bar{\bar{\theta}}$ are shown in Fig. 14. The optimiser has the ability to match the FS shapes well, however the results are jeopardised by the poor conditioning of the reference curves at the tip; this is attributed to the incremental change in stiffness at the the FS rotor's blade tip as well as the sensitivity of the section to warping, as outlined in Section II.B.2. The equality constraint on tip displacement ultimately leads to a stiffer structure, as manifested by the reduced displacement magnitude, compromising the optimisation results.

IV. Conclusion

The present paper presents a novel modelling methodology as well as a template for the design of an aeroelastically scaled WT model of a 2BTH wind turbine. The main findings as well as recommendations for future work are presented below.

The modelling methodology treats the 2BTH rotor as a simply supported beam at mid-span, thereby proposing a lumped parameter approximation for the EoM. This formulation is compatible with simple aerodynamic models such as strip theory, laying the foundation for a low fidelity aeroelastic model. The proposed approximations for the structural, rotordynamic and geometric stiffness terms were validated numerically. The ROM of the structure showed good agreement with the FE shell model in terms of natural frequencies, as long as the corresponding modeshapes

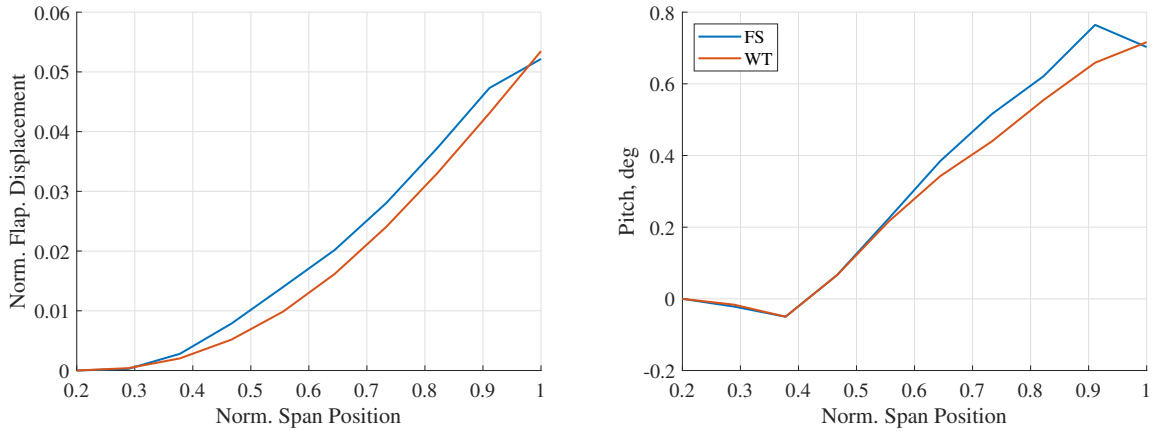

Figure 14 Normalised static displacement

do not feature excessive localised deformation, which is the case after the 9th mode. Regarding rotordynamics and geometric stiffness, analytical expressions were derived for $[K_{CE}]$, $[B_{CO}]$ and $[K_{GE}]$. It was found that in the context of the FS model, the effect of $[K_{CE}]$ and $[B_{CO}]$ is negligible, as a result of the structure's relatively high stiffness and low inertia characteristics. In contrast, the effect of $[K_{GE}]$ was found to be significant, warranting its inclusion in the EoM.

The proposed scaling methodology is tailored to the practical limitations imposed by the boundary conditions of the project, namely the choice of wind tunnel and the use of the provided test rig and rotor hub. The methodology features a decoupled two-step optimisation, addressing aerodynamics and structural design separately, by matching the respective Π_i. In terms of aerodynamics, this was largely achieved by maintaining the normalised chord and twist distribution, along with λ. Changing the airfoil from the 18% t/c NACA63618 to the 14% t/c SD7062, improved the match between the aerodynamic polars of the WT and FS model and hence the match in terms of $\bar{\bar{\Gamma}}$, Lo, C_T and C_P, which are functions of C_L and C_D. The use of transition strips was also recommended. With regards to structural design, an inevitable mismatch in Lo due to manufacturability constraints on minimum allowable feature thickness, lead to the development of two separate blade design templates. The stiff blades aim to match vibration behaviour, whereas the flexible blades match static displacement. Both templates were designed to be 3D-printable as a single part, only requiring the application of Oralight foil to complete the assembly. The templates are split into spanwise and chordwise partitions of constant thickness, to be tailored during design optimisation. Separate optimisation frameworks were designed, each addressing the purpose of the respective blades. Regarding the stiff rotor, an equality constraint was enforced for $\bar{\bar{\omega}}_{F1S}$, $\bar{\bar{\omega}}_{F2S}$ and $\bar{\bar{\omega}}_{TO1}$, which was achieved within 2.7% error; this was not the case for $\bar{\bar{\omega}}_{E1}$, while modeshapes and anti-symmetric modes were also not considered. The flexible rotor showed the ability to capture $\bar{\bar{\bar{x}}}$ and hence the structure's target stiffness at significantly reduced mass, however the quality of the match was compromised by unrealistic discontinuities in the reference shape, accentuated by the enforced equality constraint on tip displacement.

Future work will focus on a variety of topics. First, some of the limitations of the present study will be addressed, starting with the differences in hub modelling; this entails the use of a realistic, detailed design of the FS hub structure along with a new design for a flexible WT hub which will be subjected to design optimisation. Having tackled this source of mismatch, the optimiser design will be refined to include the consideration of $\bar{\bar{\bar{\phi}}}_n$ and anti-symmetric modes in the stiff blades and to remove the equal tip displacement constraint in the flexible blades. Overall, these changes are anticipated to improve the quality of the match between FS and WT rotors. Second, a strip theory aerodynamic model will be coupled to the ROM, thereby establishing a rotordynamic-aeroelastic model of the 2BTH rotor. Finally, wind tunnel tests are scheduled, which will offer an opportunity to manufacture the derived rotor designs and assess the numerical models experimentally.

Acknowledgments

The authors acknowledge support from the Rijksdienst voor Ondernemend Nederland (RVO) through the TSE Hernieuwbare Energie funding scheme for the project "TouchWind-PoP: Proof of principle for cost-effective floating offshore wind turbine concept" (TEHE119017).

References

[1] Global Wind Energy Council, "Floating Offshore Wind - A Global Opportunity," , March 2022. URL https://gwec.net/floating-offshore-wind-a-global-opportunity/.

[2] "TouchWind," , (n.d.). URL https://touchwind.org/technology/, [Last Accessed: 2022-11-23].

[3] Glauert, H., "The theory of the autogyro," *The Journal of the Royal Aeronautical Society*, Vol. 31, No. 198, 1927, p. 483–508. https://doi.org/10.1017/s0368393100133206.

[4] Schepers, J. G., "An engineering model for yawed conditions, developed on basis of wind tunnel measurements," *37th Aerospace Sciences Meeting and Exhibit*, 1999. https://doi.org/10.2514/6.1999-39.

[5] Wright, A., Osgood, R. O., and J, M. D., "Analysis of a two-bladed, teetering-hub turbine using the ADAMS software," *Windpower '94*, 1994.

[6] Bergami, L., Aagaard Madsen, H., and Rasmussen, F., "A Two-Bladed Teetering Hub configuration for the DTU 10 MW RWT: loads considerations," *Proceedings of EWEA 2014*, 2014.

[7] Civati, M., Sartori, L., and Croce, A., "Design of a two-bladed 10 MW rotor with teetering hub," *Journal of Physics: Conference Series*, Vol. 1037, 2018. https://doi.org/10.1088/1742-6596/1037/4/042007.

[8] Bottasso, C. L., Campagnolo, F., and Petrović, V., "Wind tunnel testing of scaled wind turbine models: Beyond aerodynamics," *Journal of Wind Engineering and Industrial Aerodynamics*, Vol. 127, 2014, pp. 11–28. https://doi.org/https://doi.org/10.1016/j.jweia.2014.01.009.

[9] Canet, H., Bortolotti, P., and Bottasso, C. L., "On the scaling of wind turbine rotors," *Wind Energy Science*, Vol. 6, 2021, pp. 601–626. https://doi.org/https://doi.org/10.5194/wes-6-601-2021.

[10] Krishnan, N., Viré, A., and van de Klippe, R., "Study of a passive pitching rotor using blade element momentum theory coupled to a rigid-body model," *Journal of Physics: Conference Series*, 2022. https://doi.org/10.1088/1742-6596/2265/3/032057.

[11] Shirzadeh, R., Devriendt, C., Bidakhvidi, M. A., and Guillaume, P., "Experimental and computational damping estimation of an offshore wind turbine on a monopile foundation," *Journal of Wind Engineering and Industrial Aerodynamics*, Vol. 120, 2013, pp. 96–106. https://doi.org/https://doi.org/10.1016/j.jweia.2013.07.004.

[12] Theodorsen, T., "Report No. 496, General Theory of Aerodynamic Instability and the Mechanism of Flutter," 1935. https://doi.org/https://doi.org/10.1016/s0016-0032(35)92022-1.

[13] Guyan, R. J., "Reduction of Stiffness and Mass Matrices," *AIAA Journal*, Vol. 3, No. 2, 1965, p. 380–380. https://doi.org/10.2514/3.2874.

[14] Shah, S. J., and Pilkey, W. D., "Lumped-Parameter Approach to Stability Analysis," *Journal of Engineering Mechanics*, Vol. 119, 1993. https://doi.org/https://doi.org/10.1061/(ASCE)0733-9399(1993)119:10(2109).

[15] Senjanović, I., Vladimir, N., and Cho, D. S., "A simplified geometric stiffness in stability analysis of thin-walled structures by the finite element method," *International Journal of Naval Architecture and Ocean Engineering*, Vol. 4, No. 3, 2012, pp. 313–321. https://doi.org/https://doi.org/10.2478/IJNAOE-2013-0099.

[16] Buckingham, E., "On Physically Similar Systems; Illustrations of the Use of Dimensional Equations," *Phys. Rev.*, Vol. 4, 1914, pp. 345–376. https://doi.org/10.1103/PhysRev.4.345.

[17] Selig, M., Guglielmo, J., Broeren, A., and Giguere, P., *Summary of Low-Speed Airfoil Data*, SoarTech Publications, Virginia, 1995.

[18] Drela, M., "XFOIL: An Analysis and Design System for Low Reynolds Number Airfoils," *Low Reynolds Number Aerodynamics*, Springer Berlin Heidelberg, 1989, pp. 1–12. https://doi.org/10.1007/978-3-642-84010-4_1.

[19] "Oralight," , (n.d.). URL https://www.oracover.de/film/oralight/oralight-light-iron-on-film---width_-60-cm---length_-2-m, [Last Accessed: 2022-11-23].

[20] Avin, O., Raveh, D. E., Drachinsky, A., Ben-Shmuel, Y., and Tur, M., "An Experimental Benchmark of a Very Flexible Wing," *AIAA Scitech 2021 Forum*, 2021. https://doi.org/10.2514/6.2021-1709.